

GT2014-25474

FLUTTER ANALYSIS FOR TURBOMACHINERY USING VOLTERRA SERIES

Meng-Sing Liou

Aeropropulsion Division
NASA Glenn Research Center
Cleveland, OH 44135
Email: meng-sing.liou@nasa.gov

Weigang Yao*

NASA Postdoctoral Program
NASA Glenn Research Center
Cleveland, OH 44135
Email: w.yao@qub.ac.uk

ABSTRACT

The objective of this paper is to describe an accurate and efficient reduced order modeling method for aeroelastic (AE) analysis and for determining the flutter boundary. Without losing accuracy, we develop a reduced order model based on the Volterra series to achieve significant savings in computational cost. The aerodynamic force is provided by a high-fidelity solution from the Reynolds-averaged Navier-Stokes (RANS) equations; the structural mode shapes are determined from the finite element analysis. The fluid-structure coupling is then modeled by the state-space formulation with the structural displacement as input and the aerodynamic force as output, which in turn acts as an external force to the aeroelastic displacement equation for providing the structural deformation. NASA's rotor 67 blade is used to study its aeroelastic characteristics under the designated operating condition. First, the CFD results are validated against measured data available for the steady state condition. Then, the accuracy of the developed reduced order model is compared with the full-order solutions. Finally the aeroelastic solutions of the blade are computed and a flutter boundary is identified, suggesting that the rotor, with the material property chosen for the study, is structurally stable at the operating condition, free of encountering flutter.

NOMENCLATURE

a	Speed of sound.
\mathbf{A}	Area vector.
c	Blade chord length.
C_p	Specific heat at constant pressure.
\mathbf{d}	structural deformation vector.
E	Specific total energy.
\mathbf{F}_m	Modal force vector.
\mathbf{F}	Inviscid flux vector.
\mathbf{F}^v	viscous flux vector.
$h_m(n)$	m^{th} -order Volterra series kernel.
\mathbf{K}	Stiffness matrix.
L	Length measured in the x-direction.
\mathbf{M}	Mass matrix.
M_∞	Freestream Mach number.
p	Pressure.
$P_{\kappa(\omega)}$	Turbulence production in the $\kappa(\omega)$ equation.
Pr	Prandtl number.
q_i	Heat flux vector.
q_∞	Dynamic pressure($=\rho_\infty a_\infty^2$)
\mathbf{U}	Conservative variables.
\vec{r}	Position vector.
Re	Reynolds number.
\mathbf{S}	Source term.
T	Temperature.
U_∞	Inflow velocity magnitude.
u_i	Cartesian velocity components.
x, y, z	Axial (horizontal), spanwise and vertical direction.
δ_{ij}	Kronecker delta.
ξ, η	Modal displacement.

*Currently School of Mechanical and Aerospace Engineering, Queen's University, Belfast, UK.

©This material is declared a work of the U.S. Government and is not subject to copyright protection in the United States. Approved for public release; distribution is unlimited.

κ	Turbulence kinetic energy.
μ	Viscosity.
ω	Specific turbulence dissipation rate.
Ω	Rotating speed.
σ	Value of step function.
τ	Pseudo time.
$\tau_{i,j}$	Viscous stress tensor.
\mathcal{V}	Control volume.

Subscripts

A	Aerodynamic.
∞	Far upstream or “free” stream.
m	Modal coordinate
s	Structural dynamics.
t	Total (stagnation) condition.
$turb$	Turbulence.

1 INTRODUCTION

NASA is considering new generations of aircraft that meet aggressive economic, noise and environmental targets; a special configuration, called N3-X, employs all electric power and propulsion systems by which the thrust force for the vehicle is generated exclusively with an array of fans housed in compartmentalized flow paths. Hence, the designing of fans to meet essential considerations is paramount. Specifically, increasing performance and operating life and reducing weight to optimize the economic objective, while reducing noise and emission to meet environmental regulations. In pursuit of higher performance of a compressor/fan, the past design trend is to run at higher pressure ratios and higher mass flow rates, thus moving close to flutter boundaries associated with surge or choke as defined in the compressor map. Hence, it is important to ensure the compressor is structurally sound over the entire operating range, from the choke to the stall conditions. Structural vibration, either caused by natural resonance or forced response, is a major consideration in assessing the device’s structural integrity. The fluid-induced instability of a compressor blade is typically not of concern unless it is tuned to the natural vibration frequency. However, it becomes an issue in transonic speed regime, because a small disturbance can result in a large amplitude variation and nonlinear behavior. The unsteady excursion of a shock wave through the blade-to-blade passage can intermittently choke or stall the flow, potentially crossing the flutter boundary. The unsteady forces resulting from the shock motion are shown to have either stabilizing or destabilizing effects, depending on the shock structure and inter-blade phase angle. [1]

With advances in computers and computational fluid dynamics (CFD), aeroelastic analysis is fast becoming common for real world designs. To be useful and adopted in practice, a computational tool must be reliable for predicting the aeroelastic characteristics and just as importantly be efficient (cheap and fast). This computational tool will consist of an aerodynamics code

and a structural dynamics code, as a result they in turn determine the reliability and efficiency of the tool.

For aerodynamics analysis, developments in computational fluid dynamics over the past several decades have provided increasingly powerful and reliable capabilities. The complexity and fidelity, hence its range of applicability, of analysis is strongly correlated with the fast evolution of computer power: from the early linearized potential flow solution to the current large eddy simulations using Navier-Stokes equations. Linear models are still used widely in the design phase. But developments in computer technology and CFD methods and software have made use of high-fidelity models feasible even in early stage of a design cycle. However, large eddy simulations are still far too costly and from being timely to be adopted in the design process.

In the current study, we employ the Reynolds-average Navier-Stokes equations for which the turbulence terms are closed with the two-equation κ - ω model, specifically the shear stress transport (SST) version by Menter [2]. The second-order backward differencing is used for time-discretization. The nonlinear inviscid terms are approximated by the AUSM⁺-up [3] method while the viscous terms approximated by the usual centered formulas. The resulting implicit algebraic system is then solved by the LUSGS method [4].

For structural dynamics, one may invoke the full finite element analysis, as employed in the aeroelastic study of rotor 67 by Doi [5]. The resulting fluid-structure system is a time dependent set of equations describing not only the flow variables in the entire domain, but also the motion of the structure immersed in the fluid. The system can be solved either in the frequency [6] or time domain [5]. The frequency domain approach may be preferred for linear problems for its computational efficiency; however for a nonlinear problem, it is more efficient and accurate to arrive at solution with the time domain approach.

The time-domain computation for flutter analysis can become costly when a large number of time-dependent solutions of the fluid-structure system are needed, for example as part of a design process. It is therefore desirable to reduce the computational cost by a significant factor, for example by at least an order of magnitude or more. This can be readily achieved by employing strategies called model order reduction (MOR), of which the harmonic balance, proper orthogonal decomposition, and Volterra series are among the most popular. [7] Model order reduction should not only save computational effort, but also retain the fidelity of the original (full) system. This goal has been well realized for linear problems through model reduction, but not yet universally for nonlinear problems.

For nonlinear problems, the Volterra series expansion is used to approximate the input-output relationship of a nonlinear time dependent system, with a capability of capturing “memory” effects. This input-output concept is well suited for the aeroelastic analysis in which the aerodynamic force and structural deforma-

tion can be formulated in this framework. Furthermore, flowfield and structural dynamics have different time scales and their interactions often respond with delay in time, i.e., with "memory" effects. The Volterra series has been applied in various fields of engineering and is mostly used to construct a reduced order model to mimic a complex dynamic system. Unsteady aerodynamic force responses to wing motion have been calculated by Silva [8] using the Volterra theory. In the present work, we describe the application of the Volterra series, based on RANS solutions, to turbomachinery aeroelastic problems.

The paper is organized as follows. Section 2 gives the fluid and structure equations employed and outlines the methods adopted to solve them, especially including detailed description of fluid-structure coupling and model order reduction based on the Volterra series. Section 3 presents the application to aeroelastic analysis for NASA's rotor 67 compressor blade along with the validation of the CFD solution against measured data. In Section 3.2 we show the results of applying the developed reduced-order model to find the flutter boundary of rotor 67.

2 MATHEMATICAL SYSTEM

The mathematical system considered for predicting the flutter conditions consists of the fluid and structure equations, as described in two respective sections.

2.1 Fluid Equations

The three-dimensional Reynolds-averaged Navier-Stokes (RANS) equations are employed, with the turbulence described by the two-equation κ - ω SST model [2]. They are written in the following integral form over a control volume $\mathcal{V}(\mathbf{x}, t)$ enclosed by a control surface $\partial\mathcal{V}(\mathbf{x}, t)$:

$$\frac{d}{dt} \int_{\mathcal{V}} \mathbf{U} dV + \oint_{\partial\mathcal{V}} (\mathbf{F} + \mathbf{P}) \cdot d\mathbf{A} = \oint_{\partial\mathcal{V}} \mathbf{F}^v \cdot d\mathbf{A} + \int_{\mathcal{V}} \mathbf{S} dV \quad (1)$$

where we have the standard notation for the conservative variables plus the turbulence variables in \mathbf{U} . The surface integral on $\partial\mathcal{V}(\mathbf{x}, t)$ consists of fluxes through the vectorial area $d\mathbf{A}$ can be expressed in terms of 3 Cartesian coordinates. The relative convective flux \mathbf{F}_i , the pressure flux \mathbf{P}_i , and the viscous stresses and heat flux \mathbf{F}_i^v in the i -direction, $i = 1, 2, 3$ are given in Eq. (2-3), written in the relative coordinate system moving with the speed \vec{u}_g . [9] The source terms includes the rigid-body rotation, Eq. (4)

and turbulence generation.

$$\mathbf{U} = \begin{pmatrix} \rho \\ \rho u_1 \\ \rho u_2 \\ \rho u_3 \\ \rho E \\ \rho \kappa \\ \rho \omega \end{pmatrix}, \quad \mathbf{F}_i = \begin{pmatrix} \rho(u_i - u_{g_i}) \\ \rho(u_i - u_{g_i})u_1 \\ \rho(u_i - u_{g_i})u_2 \\ \rho(u_i - u_{g_i})u_3 \\ \rho(u_i - u_{g_i})E + \rho u_i \\ \rho(u_i - u_{g_i})\kappa \\ \rho(u_i - u_{g_i})\omega \end{pmatrix}, \quad \mathbf{P}_i = \begin{pmatrix} 0 \\ \rho \delta_{i1} \\ \rho \delta_{i2} \\ \rho \delta_{i3} \\ 0 \\ 0 \\ 0 \end{pmatrix}, \quad (2)$$

and the terms attributed to viscous diffusion

$$\mathbf{F}_i^v = \begin{pmatrix} 0 \\ \tau_{i1} \\ \tau_{i2} \\ \tau_{i3} \\ \tau_{ij}u_j + q_i \\ q_{\kappa_i} \\ q_{\omega_i} \end{pmatrix}, \quad \mathbf{S} = \Omega \begin{pmatrix} 0 \\ 0 \\ -\rho u_3 \\ \rho u_2 \\ 0 \\ P_{\kappa} \\ P_{\omega} \end{pmatrix}, \quad (3)$$

Here the subscript "i" denotes the direction in Cartesian coordinates, e.g., $\mathbf{F} = \sum_{i=1}^3 \mathbf{F}_i \mathbf{e}_i$. For turbomachinery applications, the coordinate x_1 is chosen to be aligned with the rotor axial direction, and the grid velocity follows a rigid body rotation with $\Omega \vec{i}$,

$$\vec{u}_g = \vec{r} \times \Omega \vec{i} = \Omega(z\vec{j} - y\vec{k}) \quad (4)$$

It is noted that in the aeroelastic calculation performed in this study, the position vector $\vec{r}(t)$ of a computational cell varies with time as the blade geometry changes, even though the rotating speed remains fixed.

The above viscous stress terms include both the laminar and turbulent effects through the use of eddy viscosity (μ_t, k_t) model, expressed as:

$$\begin{aligned} \tau_{ij} &= (\mu + \mu_{turb}) \left[\frac{\partial u_i}{\partial x_j} + \frac{\partial u_j}{\partial x_i} - \frac{2}{3} \frac{\partial u_k}{\partial x_k} \delta_{ij} \right] \\ q_i &= -\left(\frac{\mu}{Pr} + \frac{\mu_{turb}}{Pr_{turb}} \right) \frac{\partial T}{\partial x_i} \end{aligned} \quad (5)$$

The turbulence eddy viscosity for the study presented herein is provided through the solution of two transport equations of scalar quantities (κ, ω), specifically the so-called κ - ω turbulence model [10] is enhanced with Menter's shear-stress transport (SST) model [2]. The details of the turbulence model, well-known and elaborated in the cited reference, are omitted here.

2.2 CFD Solution Methods

To eliminate accumulative time integration error, we opt for the dual-time stepping approach, in which a time rate of change

of \mathbf{U} in pseudo time (τ) is added to Eq. (1) so that at each new time level the unsteady CFD equations are balanced, namely driving its discretized residual to diminish. The dual time stepping strategy is formulated as:

$$\begin{aligned} \frac{d}{d\tau} \int_{\mathcal{V}} \mathbf{U} dV &= \mathbf{R}(\mathbf{U}) \\ &= -\frac{d}{dt} \int_{\mathcal{V}} \mathbf{U} dV - \oint_{\partial\mathcal{V}} (\mathbf{F} + \mathbf{P}) \cdot d\mathbf{A} + \oint_{\partial\mathcal{V}} \mathbf{F}^v \cdot d\mathbf{A} + \int_{\mathcal{V}} \mathbf{S} dV \end{aligned} \quad (6)$$

In the physical time step (t) the residual $\mathbf{R}(\mathbf{U})$ is discretized implicitly using a 3-level, backward differencing in order to obtain second-order temporal accuracy, resulting in a highly nonlinear system. In the pseudo-time step the implicit system is solved by performing fixed-point iterations until the residual $\mathbf{R}(\mathbf{U})$ of the nonlinear physical-time equation has diminished or reduced to specified small values. Then the solution is advanced to the next time level. This pseudo-time iteration is carried out by employing the LUSGS method [4].

The inviscid flux terms $\mathbf{F} + \mathbf{P}$ arguably have received the most attention in past CFD research, especially those under the framework of upwind solvers, yielding many proposed schemes for approximating it. In this study, We employ the AUSM⁺-up method [11] for the inviscid fluxes. For the viscous terms \mathbf{F}^v and source \mathbf{S} terms, a typical centered representation is used.

The mesh velocity is obtained from the structural motion in response to the aerodynamic forces provided by the CFD solution. The structural model is described in the next section.

The resulting in-house 3D RANS code has been developed and validated for a variety of flow problems over a number of years. For the validation relevant to the problem at hand will be described Section 3.1.

2.3 Structural Dynamics Equation

The finite element model for describing a structural motion is expressed in terms of its displacement ξ from a neutral position (steady state in our case). In our work, we first carry out finite element analysis on a given set of nodes via MSC/Nastran [12] to obtain mode shapes, $\Phi_i, i = 1, 2, \dots, N_m, N_m$ being the number of modes. Neglecting damping, the structural motion in terms of the modal displacement vector $\xi = \{\xi_i; i = 1, \dots, N_m\}$ in response to the modal force \mathbf{F}_m can be described by

$$\mathbf{M}\ddot{\xi} + \mathbf{K}\xi = \mathbf{F}_m \quad (7)$$

where (\mathbf{M}, \mathbf{K}) are the mass and stiffness matrices of the material of the structure respectively. The modes on the FEM nodes are then interpolated to every CFD node at which the aerodynamic forces are known. This modal information facilitates the

determination of the modal (generalized) force $\mathbf{F}_m = \{F_{m_i}; i = 1, \dots, N_m\}$, where each component of the modal force is the inner product of the mode shape Φ_i and aerodynamic force vectors over the entire CFD nodes. Additionally, the physical deformation \mathbf{d} of a structure can be expressed in terms of the mode shape and the modal displacement ξ from the above dynamics equation, leading to physical displacement, $\mathbf{d} = \sum_{i=1}^{N_m} \Phi_i \xi_i$ and physical force $\mathbf{f} = \sum_{i=1}^{N_m} \Phi_i F_{m_i}$.

The above second-order differential equation can be recast into the following first-order differential system:

$$\dot{\eta} = \mathbf{A}_s \eta + \mathbf{B}_s \mathbf{F}_m \quad (8)$$

where

$$\eta = \begin{bmatrix} \xi \\ \dot{\xi} \end{bmatrix}, \quad \mathbf{A}_s = \begin{bmatrix} \mathbf{0} & \mathbf{I} \\ -\mathbf{M}^{-1}\mathbf{K} & \mathbf{0} \end{bmatrix}, \quad \mathbf{B}_s = \begin{bmatrix} \mathbf{0} \\ -\mathbf{M}^{-1} \end{bmatrix} \quad (9)$$

and $\eta = \{\eta_i; i = 1, \dots, N_m\}$.

The time derivative in Eq. (8) is approximated by the second-order Crank-Nicolson method, producing a discrete system for $t^n \leq t \leq t^{n+1}$,

$$\eta(n+1) = (\mathbf{I} - 0.5\Delta t \mathbf{A}_s)^{-1} ((\mathbf{I} + 0.5\Delta t \mathbf{A}_s) \eta(n) + \mathbf{B}_s \mathbf{F}_m(n)) \quad (10)$$

This will form part of the coupled fluid-structure (aeroelastic) system to be elaborated below. It specifically provides the time-dependent modal displacement ξ , hence the needed physical displacement of the structure so as to affect fluid flow in response to the geometry variations. The mathematical system describing the interactions between fluid and structural dynamics is given below.

2.4 Fluid-Structural Coupling

The coupling of aerodynamic and structural computations must be performed on a common geometry, while they need not be of the same mesh density or matching at the same grid points, as displayed in Fig. 1 for the NASA rotor 67 blade, which is the structure that will be considered in this paper. As such, interpolation/extrapolation procedures must be employed to accomplish the mapping between them, through which the proper transfer of relevant variables may be carried out. In our case, the structure deformation provides a new body to the CFD process, thus affecting boundary condition and the flow domain mesh. On the other hand, the aerodynamic force needs to be transferred to the contact points for the finite element analysis. This mapping of grids must satisfy certain physical requirements, such as conservation of virtual work, and numerical requirements of accuracy and stability.

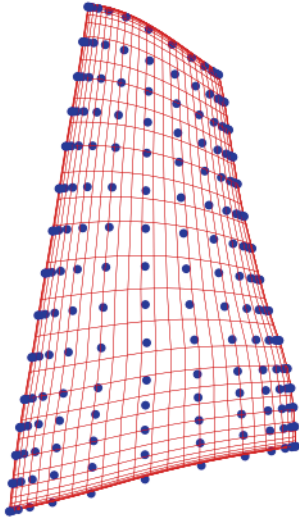


FIGURE 1: ILLUSTRATION OF GRIDS USED FOR AERODYNAMIC AND STRUCTURAL ANALYSES. BLUE: STRUCTURAL GRID; RED: AERODYNAMIC GRID. TYPICALLY THE STRUCTURAL GRID IS MUCH COARSER.

The constant volume transformation method [13] was attempted to interpolate/extrapolate between the aerodynamic and structural grids, but it failed to provide a stable and converged solution because of severe geometrical twisting involved in the present case. Instead, we employed a surrogate model to provide the structural mode shapes.

The radial-based function (RBF) neural network method, which we previously used for reduced-order modeling of flutter and limit cycle oscillations [14], is applied here by taking the finite element nodes as input and modes as output via a training process by virtue of Nastran calculations. Once the training (the RBF and neurons) is accomplished, the neural network can take the aerodynamic grid as input and produce modes as output, the modes are in turn interpolated to the aerodynamic grid.

The resulting first three mode shapes are displayed in Fig. 11, revealing indeed a large deformation of the structure. Once the blade shape deformation caused by the aerodynamic force is updated as described above, then the computational mesh for CFD is changed accordingly using transfinite interpolation (TFI) at each time step. As such, it also allows physical variables to be interpolated onto the new grid in the same manner.

A typical fluid-structure coupling is performed as shown in Fig. 2, where the structural deformation is known, hence mesh generated at t^n , a subsequent CFD solution for the new time step at t^{n+1} for U^{n+1} is performed with the structural shape frozen at q^n , then it is followed by a geometry update to get q^{n+1} with the input of U^{n+1} by procedure 3. This is the so-called loosely coupling strategy, in contrast to the tightly coupling one

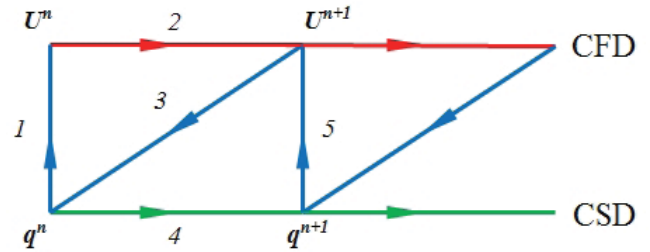


FIGURE 2: CFD AND CSD INTEGRATED COMPUTATION: LOOSE COUPLING.

in which both the CFD and computational structural dynamics (CSD) equations are solved simultaneously. The loosely coupling strategy is easy to implement and computationally efficient; the lag in time between CFD and CSD is believed to be insignificant, since the time step is usually much smaller than the characteristic time of the problem under study. This combined CFD-CSD full order modeling process is extremely expensive especially when a large number of computations are committed.

In real-world engineering practice, analysis is not performed only for one condition, but over many computations. In addition, design optimization typically will require hundreds and thousands similar computations, differing for example in range of conditions, parameters, or geometry. A reduced-order model takes only a small fraction of computational time needed by a full-order model, but is of value if and only if it is capable of preserving the accuracy of the full-order system. This can be achieved easily for a linear system, but still remains a topic of intensive research for a nonlinear system [7].

As all the aeroelastic computations for finding flutter/LCOs are similar in kind and repetitive, they differ only by a limited number of variables and the variations in value. A model order reduction will be of great value in significantly reducing computational cost and time. In what follows we will describe the application of Volterra theory [15] for constructing a reduced order model for aeroelastic analysis, based on the fidelity of the RANS equations for aerodynamic calculations.

2.5 MODEL ORDER REDUCTION BY VOLTERRA SERIES

The Volterra theory provides a functional relationship representing a nonlinear response to a given input function which may be time dependent and is capable of capturing the "memory" effect. While it has been employed in previous studies for aeroelastic application, for example [16, 17], these have been limited to external flows over an airfoil or a wing. To our knowledge, the current paper represents the first aeroelastic application of the Volterra theory to turbomachine. The Volterra theory has some

advantages over other ROMs, see [7, 17] for more discussion. The Volterra theory can be easily adopted as an alternative procedure without having to modify the baseline full-order procedure. It is equally applicable to the time and frequency domains and the conversion between them is rather simple. Moreover, the formulation facilitates to retain nonlinearity of the full order model more easily than other ROMs.

The Volterra series, unlike the Taylor series, includes in the output accumulative effects of inputs occurring at previous times. The output $y(t)$ of a continuous time-invariant system in response to a single input $u(t)$ for $t \geq 0$ is expressed by the Volterra theory as:

$$y(t) = h_0 + \sum_{i=1}^{\infty} \int_0^t \cdots \int_0^t h_i(t - \tau_1, \dots, t - \tau_i) u(\tau_1) \cdots u(\tau_i) d\tau_1 \cdots d\tau_i. \quad (11)$$

where h_0 is the steady-state term coincident with the initial condition and h_i , $i \geq 1$ are known as the Volterra kernels. As the time integral is discretized over a n -interval domain, a time-discrete infinite (or truncated) Volterra series is obtained:

$$\begin{aligned} y(n) &= h_0 + \sum_{k=0}^n h_1(n-k)u(k) \\ &+ \sum_{k_1=0}^n \sum_{k_2=0}^n h_2(n-k_1, n-k_2)u(k_1)u(k_2) + \cdots \\ &+ \sum_{k_1=0}^n \cdots \sum_{k_m=0}^n h_m(n-k_1, \dots, n-k_m)u(k_1) \cdots u(k_m) + \cdots \end{aligned} \quad (12)$$

where $y(n)$ is the output with the time index n referring to t^n , $u(k)$ is the input at preceding times $k = 0, 1, 2, \dots, n$, and h_m the m th-order Volterra kernel, $m = 1, 2, \dots, \infty$. For a linear system, it suffices to keep only the first-order Volterra kernel, hence

$$y(n) = h_0 + \sum_{k=0}^n h_1(n-k)u(k) \quad (13)$$

where h_0 corresponds to the response with zero input, or the force vector at steady state where there is no structural response. To capture behaviors varying with time variation, one must at least find the first-order kernel associated with the input at all other times. It turns out that from the continuous system, the first kernel measures the response to an impulse applied at $\tau_1 = 0$. To include nonlinear effects, higher order kernels are necessary, see Silva [8]

In the present study, we make use of the first kernel to build our reduced order model (ROM), for which the necessary step is the definition of $h_1(n)$, for $n \geq 0$, as will be illustrated below for

a system response after applying a step function,

$$\sigma(n) = \begin{cases} \sigma_0, & n > 0, \\ 0, & n = 0. \end{cases} \quad (14)$$

A small number is given to $\sigma_0 = 1.0 \times 10^{-4}$ to ensure the problem remains linear. Then, according to Eq. (13), we have the response,

$$y(n) = h_0 + \sigma_0 \sum_{k=0}^n h_1(n-k), \quad (15)$$

And the first kernel is readily available as

$$h_1(n) = \begin{cases} 0, & n = 0, \\ (y(n) - y(n-1))/\sigma_0, & n \geq 1. \end{cases} \quad (16)$$

The first equality holds because of the initial condition $y(0) = h(0)$.

In what follows we show how to construct a reduced order model that simply bases on a relationship between the structural motion and aerodynamic force, from the viewpoint of relating input and output data. This is easily facilitated within the state-space theory, as used in control theory. A linear state-space system can be represented in the following canonical form:

$$\mathbf{x}_a(n+1) = \mathbf{A}_a \mathbf{x}_a(n) + \mathbf{B}_a \xi(n) \quad (17)$$

$$\mathbf{F}_a(n+1) = \mathbf{C}_a \mathbf{x}_a(n) + \mathbf{D}_a \xi(n) \quad (18)$$

where $\mathbf{x}_a(n)$ is the state vector at time n . The input ξ is the structural displacement and the system output \mathbf{F}_a denotes the non dimensional generalized aerodynamic force.

To set up the above system and solve for the aeroelastic system under consideration, we adopt the Eigensystem Realization Algorithm (ERA) [18]. First, we define the finite Hankel matrix constructed using the first-order Volterra kernel h_1 just described above,

$$H(k-1) = \begin{bmatrix} h_1(k) & h_1(k+1) & \cdots & h_1(k+\beta-1) \\ h_1(k+1) & h_1(k+2) & \cdots & h_1(k+\beta) \\ h_1(k+2) & h_1(k+3) & \cdots & h_1(k+\beta+1) \\ \vdots & \vdots & \vdots & \vdots \\ h_1(k+\alpha-1) & h_1(k+\alpha) & \cdots & h_1(k+\alpha+\beta-2) \end{bmatrix}_{\alpha \times \beta} \quad (19)$$

where α and β are the sampling time shift in the row and column directions respectively; they control the order (rank) of the system, and are set as $\alpha = 1600$, and $\beta = 50$ in our study. Applying

Singular Value Decomposition to $H(0)$,

$$H(0) = U\Sigma V^T \quad (20)$$

we find U, Σ and V , which are then used to define the matrices in Eq. (17):

$$\begin{aligned} \mathbf{A}_a &= \Sigma^{-1/2} U^T H(0) V \Sigma^{-1/2} \\ \mathbf{B}_a &= \Sigma^{1/2} V^T E_L \\ \mathbf{C}_a &= E_M^T U \Sigma^{1/2} \\ \mathbf{D}_a &= h_1(0) \end{aligned} \quad (21)$$

where

$$\begin{aligned} E_M^T &= [I_M \ 0_M \ \cdots \ 0_M]_{\alpha M \times M} \\ E_L^T &= [I_L \ 0_L \ \cdots \ 0_L]_{\beta L \times L} \end{aligned} \quad (22)$$

with M and L being the number of inputs and outputs respectively. Since only first three modes are retained, we have $M = 3$ and $L = 3$. The size of the ROM is $3 \times \beta = 150$ for this study.

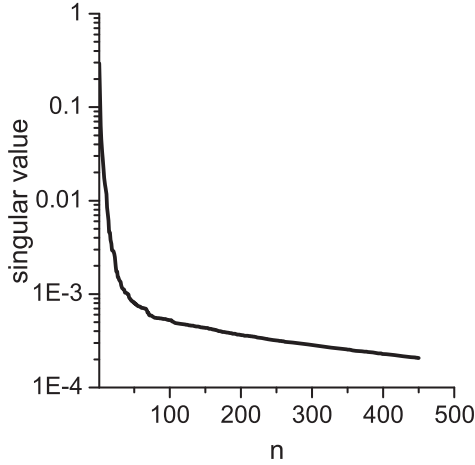


FIGURE 3: DECAY OF (NORMALIZED) SINGULAR VALUES OF THE HANKEL MATRIX.

In Fig. 3, we show the efficiency of the reduction method. Singular values of the Hankel function are seen to decay rapidly within the first 50 values, indicating that model order is of reasonable size needed to retain accuracy.

It is appropriate at this juncture to illustrate the entire aeroelastic analysis process in a flow chart shown in Fig. 4. The ROM

track starts with the baseline CFD solution as the full-order will, then builds the Volterra kernel shown in Eq. (16), which forms the state space system in Eq. (17). The input and output of which, ξ and F_a , are coupled with the structural dynamics system in Eq. (10). It is noted that $\mathbf{F}_m = q_\infty \mathbf{F}_a$, with q_∞ being the dynamic pressure ($\rho_\infty a_\infty^2$). These two systems combined form the ROM for the aeroelastic analysis discussed next.

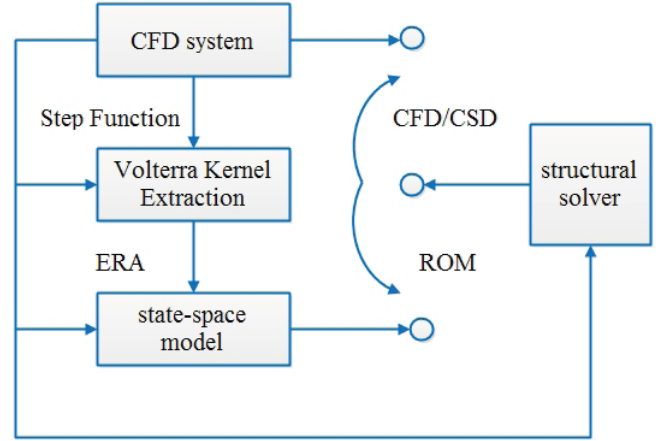


FIGURE 4: FLOW CHART ILLUSTRATING THE PROCESS OF PERFORMING AEROELASTIC ANALYSIS IN THE PRESENT STUDY.

3 Aeroelastic Analysis of NASA Rotor 67

Complex vibration problems arise from the interactions of nonlinear aerodynamics and structural deformation. These vibrations can be either self-induced or caused by flow distortions from upstream and downstream blade rows or tip region; the former is called flutter and the later forced response. Also mistuning in blade rows and inter-blade phase angle can force vibration on a blade. [19] Bendiksen [20] gives a comprehensive review of aeroelastic problems encountered in turbo machines, in which various factors causing flutter are identified. A recent discussion on the progress and challenges of computational aeroelastic modeling can be found in Bartels and Sayma. [21] Aeroelastic analyses of rotor 67 have been conducted by Doi [5], Sadeghi and Liu [22] and Zhang et al [19], employing full-order modeling of the fluid-structural system where RANS is used in the CFD procedure. An inlet guide vane row is included in Zhang et al to study its effect on the flutter characteristics. Doi found that operating condition and inter-blade phase angle determine the stability of the structural response; Sadeghi found the rotor to be stable using the 10 first eigenmodes. In our study, we also choose this rotor for our computational test model because the model reveals most flow complexities seen in the turbomachines

in today's aircraft and also widely used in the turbo machinery community for validation of CFD results, thus allowing us to verify our proposed approach for AE analysis against previous works, for example [23, 24, 5, 22].

In what follows, we shall first validate the CFD solution for detailed profiles and performance map against the measured data taken in [25]. Then the fluid-structure coupling procedure will be described, followed by the aeroelastic calculation of the blade. A model order reduction method based on the Volterra series is introduced and applied to rotor 67 to determine the flutter behavior.

3.1 Validation at Steady State Operating Points

NASA rotor 67, shown in Fig. 5 is the first stage rotor of a two-stage fan [26]. It is a low aspect ratio (1.56) transonic axial flow rotor with a design tip relative Mach number of 1.38; an experiment program was undertaken to provide laser anemometry and aerodynamic performance data at Glenn (formerly Lewis) Research Center in 1980s, culminating in an extensive compilation by Strazisar et al [25]. Shown in Fig. 6 is the test model of the rotor with 22 blades assembled. The rotor was designed for axial inflow and did not require inlet guide vanes, nor a stator stage. The design total pressure ratio is 1.63 at a mass flow rate of 33.25 kg/s (choked at 34.96 kg/s) and a rotating speed of 16,043 rpm. Other geometrical dimensions and operating conditions can be found in the cited reference. The laser anemometry measurements acquired on streamsurfaces, starting at roughly one chord length upstream of the rotor and continuing through it till some distance into the wake, providing detailed data in the form of relative Mach number and relative flow angle. Flow variables were also available at an upstream and a downstream planes. These data will be used to validate our computed results first, before building up the reduced order.

The characteristics boundary conditions are employed for the inviscid boundaries: at the subsonic inflow boundary the left running (negative) Riemann variable is extrapolated from the interior domain; at the subsonic outflow boundary the static pressure is specified at the hub and radial pressure equilibrium assumed to calculate other radial points. The no-slip conditions are applied at the hub. But the shroud in this study is assumed to be an inviscid wall (or a streamsurface), this may cause some discrepancies of our results from the data, as will be remarked when appropriate. The mesh used for the CFD solution is shown for the blade tip in Fig. 7 in an overall view and two enlarged views showing the dense mesh at the blade surface and in the wake. Similar mesh distribution is also generated for all spanwise sections. Two H-type mesh systems, one coarse and another fine, are used first to establish whether the coarse mesh is sufficiently accurate to be used for further aeroelastic analysis. The two meshes respectively consist of 77x43x45 and 104x63x80 grid points (resulting in 140,448 and 504,494 cells)—the three numbers respectively refer to the streamwise, blade-to-blade, and spanwise di-

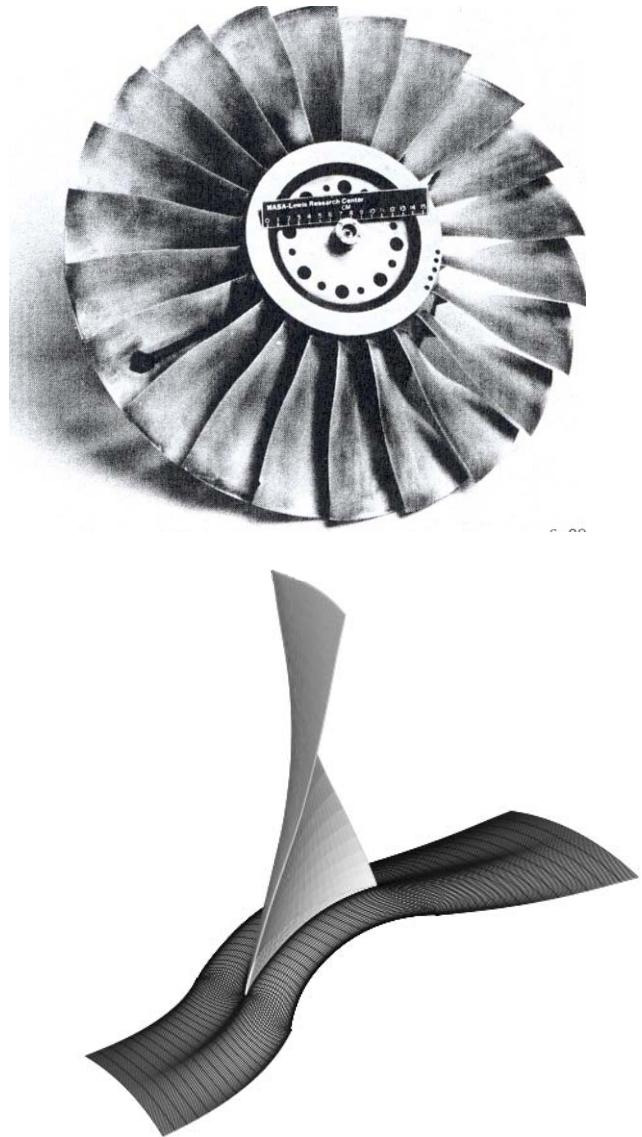


FIGURE 6: BLADE SHAPE OF THE NASA ROTOR 67 AS MOUNTED ON THE HUB, TOGETHER WITH THE ALIGNED COMPUTATIONAL SURFACE.

rections. This mesh density may be considered coarse in today's CFD practice, however, Fig. 8 shows that the computed profiles of static pressure and total pressure and temperature at the exit plane from both grids are essentially indistinguishable. These solutions are also comparable with the measured data and other published CFD results using finer meshes, for example in [5,22]. Hence we consider the coarse grid to adequate to provide sufficiently accurate aerodynamic forces to the structural analysis and thus, to be employed in this study. Moreover, our emphasis in this paper is to show the efficacy and validity of the proposed

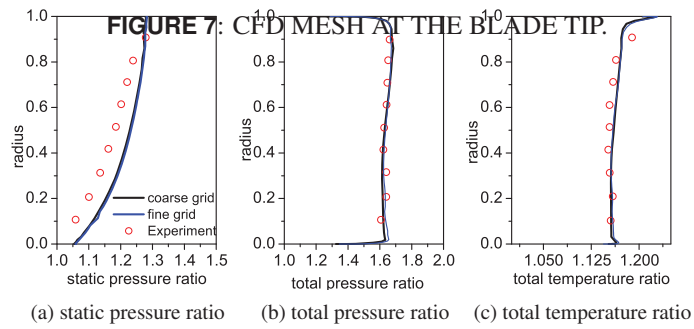
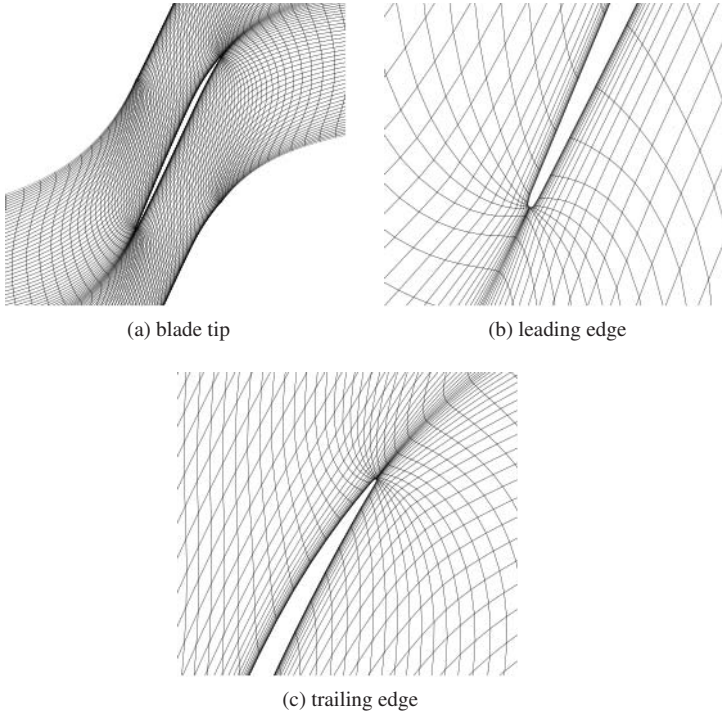


FIGURE 8: PROFILES OF STATIC PRESSURE, TOTAL PRESSURE AND TEMPERATURE RATIOS AT AN EXIT LOCATION WHEN THE ROTOR IS NEAR PEAK EFFICIENCY.

model order reduction method for AE analysis.

It is noted, however, that an overestimation is found in the static pressure ratio by the computation. This is probably caused by several simplifications committed in our computational setup: (1) we did not assume a boundary layer profile at the inflow boundary while in the experimental setup a solid surface is connected to the hub surface of the rotor, (2) the tip clearance is not taken into account and instead an inviscid slip wall is assumed at the casing, and (3) the hub wall is assumed adiabatic, hence possibly giving rise to a higher temperature or pressure in the layer at the hub. This low-momentum layer at the inlet will continue to develop, growing through the rotor, resulting in a thickened boundary layer profile, in comparison with the computed result which indicates a fuller profile in a thinner layer.

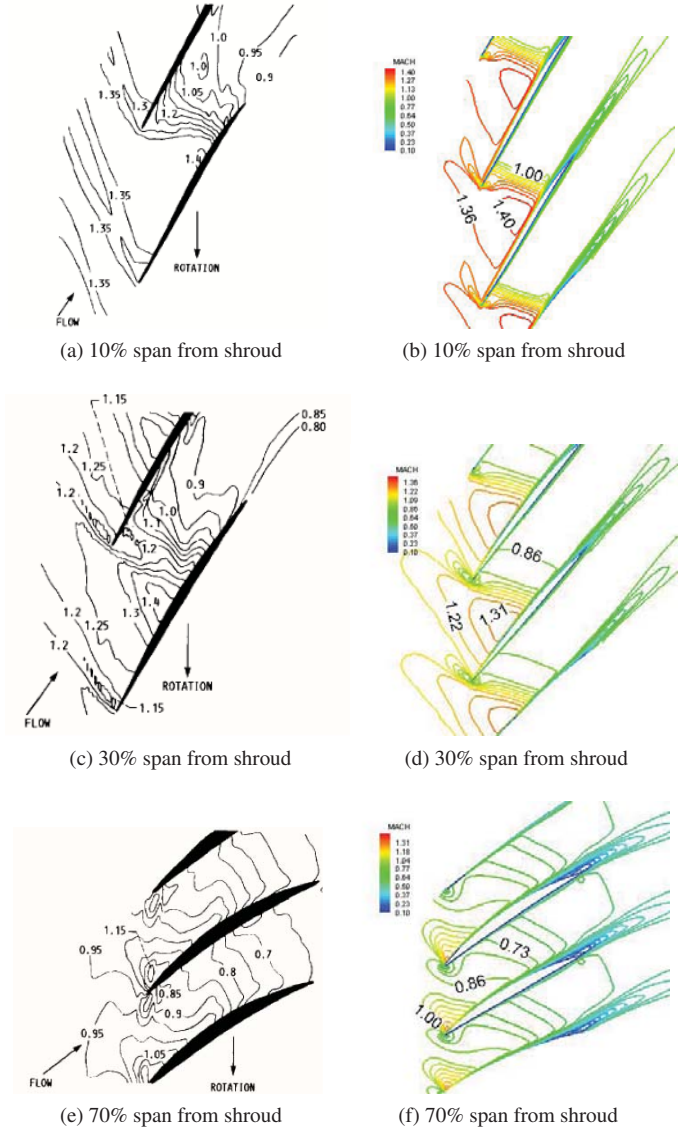


FIGURE 9: RELATIVE MACH NUMBER CONTOURS AT THREE SPANWISE SECTIONS, RESPECTIVELY 10%, 30% AND 70% MEASURED FROM SHROUD.

The relative Mach contours at three spanwise sections, respectively 10%, 30% and 70% measured from the tip, are compared for the peak efficient condition in Fig. 9, revealing the nearly normal shock wave across the blade passage at the tip section, but subsonic or low supersonic near the root.

Finally, we plot the rotor 67 performance by the CFD solution in comparison with the measured values, as shown in Fig. 10. At the peak efficiency point, the solution gives a mass flow rate of 33.68 kg/s, a total pressure ratio of 1.651, and an efficiency of 0.9178. The calculated results are in good agreement with the data over the entire operating conditions.

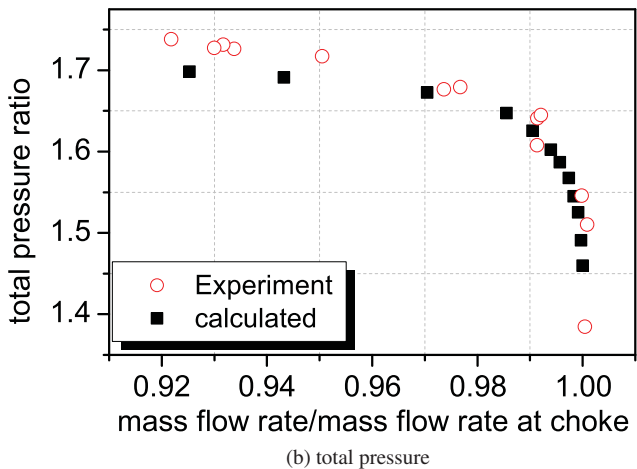
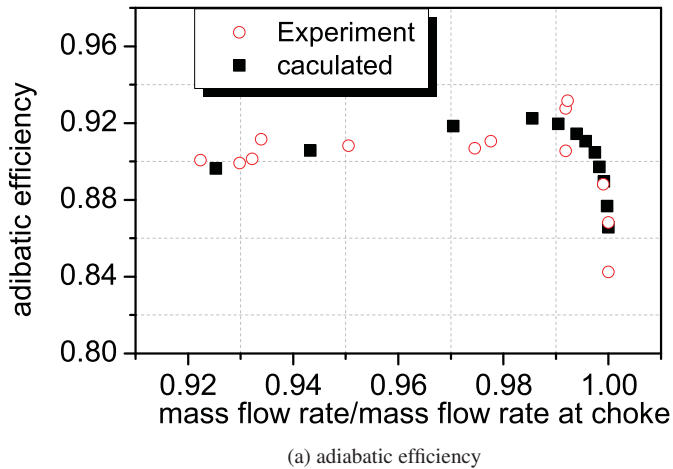


FIGURE 10: ROTOR 67 PERFORMANCE VS MASS FLOW RATIO: EFFICIENCY AND TOTAL PRESSURE RATIO.

3.2 FLUTTER ANALYSIS FOR ROTOR 67

The flutter characteristics depends on the structural properties, in addition to the aerodynamic conditions. The material chosen for consideration is titanium alloy whose properties are given in Table 1, same as those used in [5, 22]. (The material in Doi's work was altered to give the Young's modulus of 1.422×10^{11} (Pa) to place the first natural frequency away from the rotating frequency or its double.)

The first three modal frequencies, calculated with the commercial software MSC/Nastran [12] on a 15×15 mesh, are listed in Table 2, along with the results by Doi. Despite using different values of Young's modulus, these two predicted modal frequencies are quite close. These three mode shapes are shown in Fig. 11; the first mode representing the bending, second mode the second bending, and third mode the torsion.

TABLE 1: MATERIAL PROPERTIES.

Material	Young's modulus (Pa)	Poisson's ratio	Density (kg/m ³)
Titanium Alloy	1.172×10^{11}	0.3	4539.5

TABLE 2: MODAL FREQUENCY (HZ).

	1st mode	2nd mode	3rd mode
Present	369.8	1009.4	1622.9
Doi [5]	401.9	1096.0	2093.7

We now apply the model order reduction technique established above to rotor 67 at the peak efficiency condition. The time-dependent aerodynamic force is built using the above Volterra series with the first mode displacement given as:

$$\xi_1 = 5.0 \times 10^{-5} \sin \omega t \quad (23)$$

where ω is the first natural frequency of the structure.

It is noted that the small amplitude is chosen in Eq. (23) to ensure linearity assumed for the current ROM formulation. Since the flutter boundary estimated by the linear theory is independent of the perturbation magnitude, it is not critical what value is used as long as the value is small. The time step used in the time integration is chosen to be sufficiently small that time accuracy is maintained; in this study the time step is 2.0×10^{-5} (s), allowing about 30 time-intervals in the period of the highest frequency mode considered.

In Fig. 12, we validate the accuracy of the ROM-CSM model (system of Eqs. (17) and (7)), by comparing the first three modal forces of rotor 67 blade. The aerodynamic force is obtained either by solving the full Reynolds-averaged Navier-Stokes equations or by using the ROM with 150 degrees of freedom (i.e. the order of matrix \mathbf{A}_a in the state space model) for an input defined by Eq. (23). It reveals that the third mode (torsion) is most dominant and the weakest is the second mode (second bending). The close agreement between the full and reduced models confirms the accuracy of the current Volterra-series-based ROM. Discrepancy is seen in the second mode, but this mode is less important than the other two.

The aeroelastic ROM system consists of 150 degrees of freedom in the aerodynamic ROM and 6 in the structural representation (displacement and velocity), thus resulting in 156 DOF in total for the entire AE ROM. The instability critical point can be determined by increasing total density at inlet boundary. As

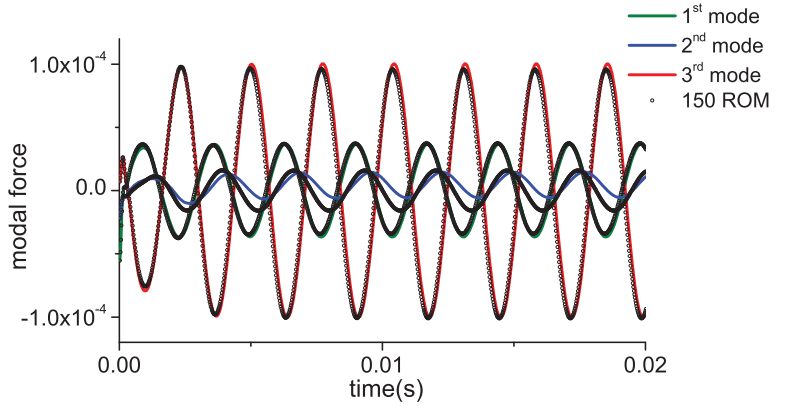
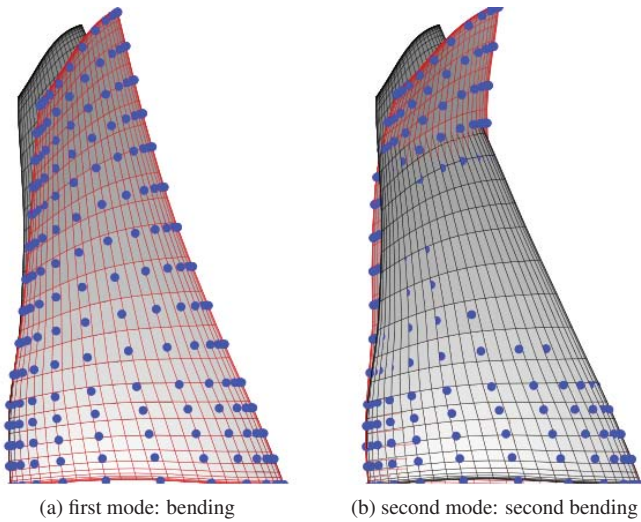


FIGURE 12: COMPARISON OF MODAL FORCE OBTAINED BY THE FULL ORDER AND REDUCED ORDER SOLUTIONS.

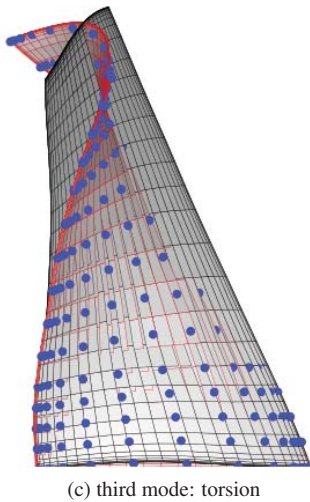


FIGURE 11: MODE SHAPES OF THE ROTOR 67 STRUCTURE AND INTERPOLATION BETWEEN THE STRUCTURAL AND AERODYNAMIC GRIDS. BLACK: NON-DEFORMED GRID; BLUE: STRUCTURAL GRID; RED: AERODYNAMIC GRID.

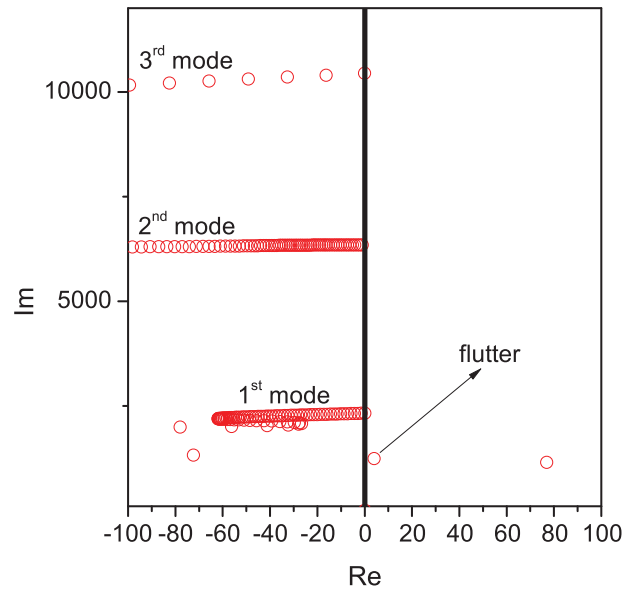


FIGURE 13: EIGENVALUES OF THE 156-ROM.

shown in Fig. 13, the 1st structural mode eigenvalue crosses the imaginary axis, i.e., the eigenvalue becomes positive, indicating an amplification of structural displacement. Figure 14 displays the blade displacement predicted by the 156 aeroelastic ROM at the flutter condition, the third and first modes are the two most dominant ones while the second mode is nearly negligible. The dynamic pressure needed to induce flutter is $q_\infty = 1.455 \times 10^6 \text{ Pa}$, nearly 10 times larger than the baseline operating condition at $q_\infty = 1.416 \times 10^5 \text{ Pa}$. Hence the rotor made with the material spec-

ified in Table 1 is determined to be structurally stable under the chosen operating condition, with a high margin of safety, when only an isolated blade is considered, this finding consistent with that in [5,22]. However, blade row interactions, such as the effect of upstream inlet guid vane, can induce forced vibration in rotor blade, thus altering its flutter characteristics, see study in [19]. The ROM strategy presented here can also serve as an efficient and reliable way of investigating the effect of inter-blade interac-

tions.

Finally we remark on the primary motivation of employing ROM, while under the foremost requirement of preserving accuracy. For performing an aeroelastic analysis over a complete sinusoidal cycle (Eq. (23)), the full-order (CFD-CSD) model takes 10.8 hours on a Xeon(R) W3530 computer with Intel(R) Compiler compared to 0.56 seconds used by the ROM, a whopping savings by over 19,200 times. This shows the tremendous value of using the ROM when searching for the flutter boundary shown in Fig. 14, or when conducting design optimization, both of which will otherwise require enormous computational resources.

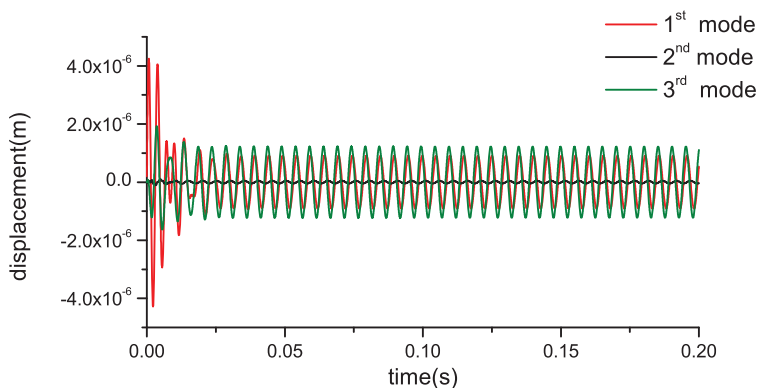


FIGURE 14: FLUTTER RESPONSE IN TERMS OF DISPLACEMENT OF THREE MODES WHERE THE TORSION AND BENDING MODES ARE DOMINANT AND THE SECOND BENDING MODE IS MINIMAL.

CONCLUDING REMARKS

We have presented an accurate and efficient method for performing aeroelastic analysis of a modern transonic compressor blade, NASA rotor 67. The CFD code, using κ - ω -SST turbulence model and AUSM⁺-up numerical fluxes, for providing aerodynamic forces has been validated against measured data. The structural motion based on finite element analysis is coupled with fluid motion. the coupling is further modeled by the state-space representation to achieve considerable reduction in computational cost, while preserving the solution accuracy. The linear state-space system is formulated by keeping only the first-order Volterra kernel. The obtained reduced order model is shown to be in excellent agreement with the full (original) model. Hence it can be employed to provide an effective aeroelastic analysis tool, specifically for defining the flutter boundary.

ACKNOWLEDGMENT

This paper presents part of the multidisciplinary design analysis and optimization (MDAO) effort contributing to the research towards next generation transport sponsored by the subsonic fixed wing (SFW) project, under the fundamental aeronautics program (FAP) in NASA's Aeronautics Mission Directorate. The authors are grateful for the support of SFW management team.

REFERENCES

- [1] Bendiksen, O. O., 1986. "Role of shocks in transonic/supersonic compressor rotor flutter". *AIAA J.*, **24**, pp. 1179–1186.
- [2] Menter, F., 1994. "Two-equation eddy-viscosity turbulence models for engineering applications". *AIAA Journal*, **32**, pp. 1598–1605.
- [3] Liou, M. S., 2006. "A sequel to AUSM, Part II: AUSM⁺-up for all speeds". *J. Comput. Phys.*, **214**, pp. 137–170.
- [4] Yoon, S. K., and Jameson, A., 1988. "Lower-upper symmetric-gauss-seidel method for the euler and navier-stokes equations". *AIAA Journal*, **26**, pp. 1025–1026.
- [5] Doi, H., 2002. "Fluid/structure coupled aeroelastic computation for transonic flows in turbomachinery". PhD Thesis, Stanford University, Stanford, CA.
- [6] Moffatt, S., and He, L., 2003. Blade forced response predictions for industrial gas turbines, Part I: methodologies. ASME Paper GT2003-38640.
- [7] Lucia, D. J., Beran, P. S., and Silva, W. A., 2004. "Reduced-order modeling: New approaches for computational physics". *Progress in Aerospace Sciences*, **40**, pp. 51–117.
- [8] Silva, W. A., 1997. Identification of linear and nonlinear aerodynamic impulse responses using digital filter techniques. AIAA Paper 1997-3712.
- [9] Chima, R. V., and Liou, M.-S., 2003. Comparison of ausm⁺ and h-cusp schemes for turbo machinery applications. 16th AIAA Computational Fluid Dynamics Conference AIAA Paper 2003-4120, Orlando, FL, 23-26 June.
- [10] Wilcox, D. C., 1988. "Reassessment of the scale-determining equations for advanced turbulence models". *AIAA J.*, **26**, pp. 1299–1310.
- [11] Liou, M.-S., 2006. "A sequel to AUSM, part II: AUSM⁺-up for all speeds". *J. Comput. Phys.*, **214**, pp. 137–170.
- [12] MSC Software Corp., 2011. *MSC/NASTRAN user manual*.
- [13] Goura, G. S. L., 2001. "Time marching analysis of flutter using computational fluid dynamics". PhD Thesis, University of Glasgow, Glasgow, UK.
- [14] Yao, W., and Liou, M.-S., 2012. Reduced-order modeling for flutter/lco using recurrent artificial neural network. AIAA Paper 2012-5446.
- [15] Volterra, V., 1959. *Theory of functionals and of integral and integro-differential equations*. Dover, New York.

- [16] Raveh, D. E., Levy, Y., and Karpel, M., 2000. Aircraft aeroelastic analysis and design using cfd-based unsteady loads. AIAA Paper 2000-1325.
- [17] Balajewicz, M., and Dowell, E., 2012. “Reduced-order modeling of flutter and limit-cycle oscillations using the sparse volterra series”. *J. of Aircraft*, **49**, pp. 1803–1812.
- [18] MathWorks Inc., 2012. *Control system toolbox manual*.
- [19] Zhang, C., Ye, Z., and Liu, F., 2009. Numerical researches on aeroelastic problem of a rotor due to igv/fan interaction. AIAA Paper 2009-865.
- [20] Bendiksen, O. O., 1990. Aeroelastic problems in turbomachines. AIAA Paper 1990-1157.
- [21] Bartels, R., and Sayma, A., 2007. “Computational aeroelastic modeling of airframes and turbomachinery: Progress and challenges”. *Phil. Trans. Royal Soc. A*, **365**, pp. 2469–2499.
- [22] Sadeghi, M., and Liu, F., 2005. Coupled fluid-structure simulation for turbomachinery blade rows. AIAA Paper 2005-0018.
- [23] He, L., and Denton, J. D., 1994. “Three-dimensional time-marching inviscid and viscous solutions for unsteady flows around vibrating blades”. *J. Turbomachinery*, **116**, pp. 469–476.
- [24] Chuang, H. A., and Verdon, J. M., 1998. A numerical simulator for three-dimensional flows through vibrating blade rows. Nasa cr 1998-208511.
- [25] Strazisar, A. J., et al., 1989. Laser anemometer measurements in a transonic axial-flow fan rotor. NASA TP 2879.
- [26] Cunnan, W. S., Stevens, S., and Urasek, D. C., 1978. Design and performance of a 427-meter-per-second-tip-speed two-stage fan having a 2.40 pressure ratio. Nasa tp-1314.